Improved electrochemical performance of $LiMn_{1.5}M_{0.5}O_4$ (M=Ni, Co, Cu) based cathodes for lithium-ion batteries

Renato Gonçalves[§,‡,*], Poonam Sharma[‖,‡], Pura Ram[‖], Stanislav Ferdov[†], M. Manuela Silva[§], Carlos M. Costa[§,†], Rahul Singhal[⊥], Rakesh K. Sharma[‖,*], Senentxu Lanceros-Méndez[#,∇]

[§]Centre of Chemistry, University of Minho, 4710-057 Braga, Portugal

[‖]Department of Chemistry, Indian Institute of Technology Jodhpur, 342011, Rajasthan, India

[†]Centre of Physics, University of Minho, 4710-057 Braga, Portugal

[⊥]Department of Physics and Engineering Physics Central Connecticut State University, New Britain, CT 06050, USA

[#]BCMaterials, Basque Center for Materials, Applications and Nanostructures, UPV/EHU Science Park, 48940 Leioa, Spain

[∇]IKERBASQUE, Basque Foundation for Science, 48013 Bilbao, Spain

Corresponding Author

[*]R.G.: e-mail, r.goncalves@quimica.uminho.pt

[*]R.K.S.: e-mail, rks@iitj.ac.in

Author Contributions

[‡]R.G. and P.S. contributed equally. The manuscript was written through contributions of all authors. All authors have given approval to the final version of the manuscript.

25   **ABSTRACT:**

26   $LiMn_2O_4$ and $LiMn_{1.5}M_{0.5}O_4$ (M: Ni, Cu, Co) doped particles have been synthetized by

27   sol-gel. Particles between 50 and 200 nm were obtained with the cubic spinel structure of

28   the $LiMn_2O_4$. Ni doping shows a more efficient substitution in the octahedral 16d site,

29   replacing the Mn^{3+} ion, improving the important drawback of poor cycling behavior of

30   $LiMn_2O_4$. The average pore size decrease with the addition of the doped elements in the

31   $LiMn_2O_4$ structure from 2.9 to 2.6 nm. Thermal analysis shows that the doped particles

32   present higher thermal stability that the undoped ones. Electrochemical behavior of the

33   cathodes prepared with each of the active materials show that the doping influenced the

34   electrochemical performance of the active material. Thus, a specific capacity of 33, 74,

35   44 and 53 mAh g^{-1} (at C) and 74, 89, 59 and 69 mAh g^{-1} (at C/10) were obtained for

36   $LiMn_2O_4$, $LiMn_{1.5}Ni_{0.5}O_4$, $LiMn_{1.5}Cu_{0.5}O_4$ and $LiMn_{1.5}Co_{0.5}O_4$ cathodes, respectively. All

37   cathodes present good electrochemical stability with low capacity fade of 0.5 and 3.1 %

38   for $LiMn_{1.5}Ni_{0.5}O_4$ and $LiMn_{1.5}Cu_{0.5}O_4$, respectively, after 50 cycles. These results show

39   an improvement of electrochemical performance for $LiMn_2O_4$ doped with Ni, Cu and Co,

40   demonstrating their suitability for lithium-ion battery systems.

41

42   **KEYWORDS:** active material; cathode; doping; lithium ion batteries; $LiMn_2O_4$

43

44

1. Introduction

The increase of portable electronic devices and hybrid electric vehicles in recent years raised the demand of high energy density energy storage systems. Lithium-ion batteries (LIBs) were first reported in 1970s and after commercialization by Sony in 1991, became the central pillar of energy storage systems because of its long lifespan, low self-discharging, high energy/power density and low memory effect. LIBs are composed by three main components: anode as a negative electrode, cathode as positive electrode and separator/electrolyte between both electrodes [1, 2]. The cathode active materials, through their characteristics lattice sites/spaces, are responsible for the lithium-ion storage/release, via electrochemical intercalation. Active cathode materials with a robust crystal structure are responsible for the cycling stability and specific capacity of the battery. Also, cathodes with high electrochemical intercalation potential and anodes, lead to high energy density batteries [3].

Cathode active materials such as Li_2MnO_3, $LiCoO_2$, $LiFePO_4$, $Li(NiCoAl)O_2$ and $LiNiO_2$, among others, are used for Li-ion rechargeable battery applications (both, commercially and under investigation) [4, 5]. One of the promising cathode active material for LIBs is spinel $LiMn_2O_4$ (LMO), that can intercalate two lithium ions in its structure. The first intercalate at 4 V (vs Li^+/Li) and the second at 3 V (vs Li^+/Li). Advantages are environmental benignity, high rate capability, high cell potential, low toxicity and low cost are associated to this structure. Nevertheless, the applicability of this structure in LIBs is limited to a capacity of 148 mAh g^{-1} at 4 V region, due to the volume expansion at 3 V region [6, 7]. This active material presents some drawbacks as a practical capacity of 120 mAh g^{-1}, reached by the $\approx 80\%$ of the lithium ions deintercalation. The fracture of the structure by the repeated cycles and the decomposition of the electrolyte (at high voltages) represent relevant disadvantages of this active material [8]. Further, this active material presents poor cycling behavior due to their fast capacity fading in the 3 V range originated by the Mn^{3+} dissolution during the lithium-ion deintercalation/intercalation and the Jahn-Teller distortion of MnO_6 octahedron at 4 V. Thus, the reduction of the Mn^{3+} ion in the $LiMn_2O_4$ spinel structure will improve the cycling performance of the batteries assembled with this active material [9]. Efforts to improve the cyclability and performance of such cathodes involve morphology control [10], coating/functionalization [11, 12], dimension reduction [13], oxygen stoichiometry [14] and doping [15]. The

78   substitution of the Mn^{3+} ion by other ions are the most efficient improvement method and

79   doping metals including Zn, Co, Fe, Cu, Ti, Mg, Al, Ni or Cr, came as a solution to

80   improve this drawback [8, 16, 17]. Furthermore, the doping with transition metals in some

81   active materials promotes the change in the oxidation state of oxygen due to the

82   deintercalation/intercalation of lithium ion into cathode during the charge/discharge

83   process. The addition of elements with multiple oxidation states should balance the

84   charge in the cathode structure during electrochemical cycling, increasing the stability

85   and specific capacity of the material [18].

86   Previous work [19] have demonstrated that the addition of rare earth elements as Gd, Nd

87   or Dy into $LiMn_{1.5}Ni_{0.5}O_4$ influence the electrochemical behavior of the active material.

88      $LiMn_{1.48}Ni_{0.5}Gd_{0.02}O_4$ shows excellent applicability in LIBs, compared with the others

89   studied active materials, at high scan-rate (C-rate) with good electrochemical

90   performance (104 mAh g^{-1} after 55 cycles at C-rate). $LiNi_{0.5}Mn_{1.5}O_4$ active material

91   surface-treated with cobalt at 500 and 700 °C allow to increase the electrochemical

92   response of LIBs [20]. Transmission electron microscopy (TEM), Raman and X-ray

93   photoelectron spectroscopy (XPS) results show that the samples treated at 700 °C creates

94   a surface layer on the active material that enhances the long cycle and high-temperature

95   cycling performance. The reason for this excellent performance is due to the cobalt layer

96   that decreases the nickel concentration and also increases the oxidation state of nickel on

97   the surface. The sample shows a capacity of 93 mAh g^{-1} after 2000 cycles at 5C-rate with

98   a capacity retention of 81%.

99   Compared with rare earth elements, the use of transition metal elements more abundant

100   in the Earth crust and less expensive, to improve the LMO drawbacks should be explored.

101   Therefore, Cu and Co doping of $LiMn_2O_4$, that are poorly studied, were achieved and

102   compared with Ni doping, which is more studied and leads to high specific capacity value.

103   Further, a sol-gel synthesis method for Ni, Cu and Co doping of $LiMn_2O_4$ is presented in

104   order to develop LIB cathode active materials for energy storage systems. With the

105   present study, the different contributions of each element have been studied and their

106   electrochemical performance evaluated, showing their potential in the energy field.

107

2. Material and methods

2.1. Particles synthesis and characterizations

$LiMn_2O_4$ and Ni, Cu and Co doped ($LiMn_{1.5}Ni_{0.5}O_4$, $LiMn_{1.5}Cu_{0.5}O_4$ and $LiMn_{1.5}Co_{0.5}O_4$, respectively) particles were synthetized via sol-gel method using precursors of lithium acetate – $LiCH_3COO$ (99.9%), manganese acetate – $Mn(CH_3COO)_2$ (99.5%), nickel acetate – $Ni(CH_3COO)_2$ (99.9%), copper acetate – $Cu(CH_3COO)_2$ (99.9%) and cobalt acetate – $Co(CH_3COO)_2$ (99.9%) (all from Alfa Aesar, USA), in their stoichiometry ratio. To reach homogeneous solutions, the precursors were dissolved in 2-ethyl hexanoic acid (99% from Merck) at a temperature between 100-150 °C, followed by stirring at 250 rpm for 30 min. As prepared powders were exposed to a heating treatment in order to achieve high purity phase and stability. More details on the synthesis process can be found in [21]. The obtained pure phase particles were then ball milled with 10:1 ball weight/material weight ratio for 6 h in a planetary high energy ball milling (Retsch PM-100 model).

Elemental analysis and surface morphology were evaluated by Scanning Electron Microscopy (SEM) using a Scanning Electron Microscope (Carl Zeiss, Evo special addition). The beam current during energy dispersive X-ray and surface morphology were 200 nA and 80 pA, respectively. Phase-contrast images were obtained by high-resolution transmission electron microscopy (HRTEM) measurements using a TEM Tecnai G2 instrument by FEI with an accelerating voltage of 200 kV. The powder's phase purity was characterized by X-ray using a Brucker D8 advance, in the range two theta angle 10°–80° with a scan rate of 0.02° per second in locked coupled mode. To evaluate the samples phase content and identification, the Rietveld method using TOPAS-3 software (Bruker AXS Inc.) and the EVA software (EVA Software, DIFFRACplus Release 2006, Bruker AXS) were used. The structural characterization was realized by Raman analysis performed with 2 mW power air-cooled LASER excitation source operating at 532 nm, using an STR 500, Airix Japan, spectrophotometer. Brunauer-Emmett-Teller (BET) surface analysis was performed using AutoSorb(iQ3), Quantunchrome Instrument, USA. Experiments were carried out using 300 mg samples that were degassed in H_2 atmosphere pressure at 300 °C for 2 h and 20 points adsorption and desorption were measured in N_2 atmosphere. Thermogravimetric measurements were performed with a TGA 4000, PerkinElmer set-up from 30 °C to 900 °C at a constant heating rate of 10 °C per minute.

2.2. Preparation and characterization of the cathodes and half-cells

The prepared powders of $LiMn_2O_4$ (LMO), $LiMn_{1.5}Ni_{0.5}O_4$, $LiMn_{1.5}Cu_{0.5}O_4$ and $LiMn_{1.5}Co_{0.5}O_4$ were used as active materials for cathode preparation. The slurry of the cathode were prepared by mixing 80% of each active material with 10% of carbon black (conductive material), 10% of poly(vinylidene fluoride) (PVDF, Solvay 5130) (binder) and N-methylpyrrolidone (NMP, Fluka) as a solvent. The electrode preparation was carried out as previously reported [19]. Briefly, PVDF was dissolved in the NMP solvent, forming the binder solution. After that, the active and conductive materials were added (dry mixing) under constant stirring. The obtained cathode slurry was spread uniformly on an aluminium metal grade foil and placed in a furnace for the evaporation of the solvent (80 °C for 2 h). Three half-cells (Swagelok) of each active material were prepared and assembled inside a home-made glove box filled with argon. For that, all the materials were dried overnight at 90 °C in vacuum. Lithium metal foil was used as anode material and the Whatman glass microfiber filters (grade GF/A) used as a separator. The electrolyte used was the 1M $LiPF_6$ salt dissolved in ethylene carbonate + dimethyl carbonate (EC + DMC, 1:1 volume percentage) from Solvionic.

Electrochemical impedance spectroscopic (EIS) studies were carried out using an Autolab PGSTAT12 instrument. The frequency range used was from 1 MHz to 10 mHz with an amplitude of 10 mV. The charge/discharge cycle tests were performed for the different half-cells with a Galvanostatic mode at different C-rates (C/10, C/5, C/2, C and 2C) between 3.5 V and 4.9 V, using a Landt CT2001A Instrument.

3. Results and Discussion
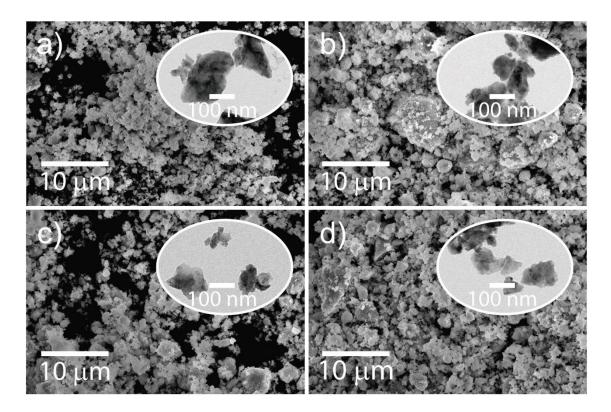
The LMO doped with nickel, copper, cobalt, and pure LMO particles were studied to characterize the doping influence on particles main characteristics and their performance as active material in lithium-ion battery systems.

3.1. Synthesized powder structural and surface morphological properties

172 Figure 1 shows powders surface morphological studies of the synthesized particles
173 evaluated by SEM and TEM. The SEM and TEM images show a similar dispersion of
174 particles size for all the samples, ranging between the 50 and 200 nm. It is possible to
175 affirm that single particles present a polyhedron shape and the existence of some bigger
176 particle due to agglomeration of these particles, confirmed by TEM images (inset Figure
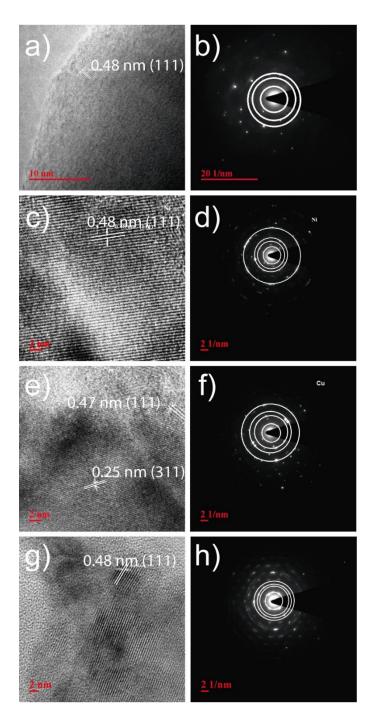177 1).

178

179 **Figure 1-** Surface morphology characterization by SEM and TEM (inset) of a) $LiMn_2O_4$,
180 b) $LiMn_{1.5}Ni_{0.5}O_4$, c) $LiMn_{1.5}Cu_{0.5}O_4$ and d) $LiMn_{1.5}Co_{0.5}O_4$ particles.

181

182 HRTEM images of the $LiMn_2O_4$, $LiMn_{1.5}Ni_{0.5}O_4$, $LiMn_{1.5}Cu_{0.5}O_4$ and $LiMn_{1.5}Co_{0.5}O_4$
183 particles (Figure 2a,c,e and g) show oriented crystals within the particles, demonstrated
184 through the identification of the lattice fringes of the cubic spinel (111) plane. It was
185 identified lattice fringes of about 0.48, 0.48, 0.47 and 0.48 nm for the single crystalline
186 domains of the $LiMn_2O_4$, $LiMn_{1.5}Ni_{0.5}O_4$, $LiMn_{1.5}Cu_{0.5}O_4$ and $LiMn_{1.5}Co_{0.5}O_4$,
187 respectively. The selected area electron diffraction (SAED) of $LiMn_2O_4$, $LiMn_{1.5}Ni_{0.5}O_4$,
188 $LiMn_{1.5}Cu_{0.5}O_4$ and $LiMn_{1.5}Co_{0.5}O_4$ particles (Figure 2b,d,f and h) show an inner and
189 intense circle at (111) plane, followed by others rings at (311) and (400).

Figure 2- HRTEM and SAED images for a-b) $LiMn_2O_4$, c-d) $LiMn_{1.5}Ni_{0.5}O_4$, e-f) $LiMn_{1.5}Cu_{0.5}O_4$ and g-h) $LiMn_{1.5}Co_{0.5}O_4$ particles.

Elemental analysis of the particles was performed by SEM-EDX and the chemical composition results are summarized in Table 1. The elemental atomic composition for the studied samples is similar to the stoichiometric ratio, showing the success of the doping method applied to the $LiMn_2O_4$ particle.

198 **Table 1** – Elemental atomic composition obtained from the SEM-EDX for $LiMn_2O_4$ and

199 $LiMn_{1.5}M_{0.5}O_4$ (M: Ni, Cu, Co) doped particles.

Sample description	Elemental Atomic (%)		
	Mn	O	M (Ni, Cu, Co)
$LiMn_2O_4$	33.44	66.56	0.0
$LiMn_{1.5}Ni_{0.5}O_4$	25.73	67.06	7.21
$LiMn_{1.5}Cu_{0.5}O_4$	28.52	62.69	8.79
$LiMn_{1.5}Co_{0.5}O_4$	26.17	65.06	8.77

200

201 To study the phase purity and lattice size of the powders, XRD patterns were analyzed.
202 The results of XRD analysis (Figure 3) show only the characteristics reflection peaks of
203 the cubic structure of spinel $LiMn_2O_4$ with Fd-3m space group and the lattice planes of
204 (111), (311), (222), (400), (331), (511), (440) and (531) (JCPDS File No. 35- 0782), in
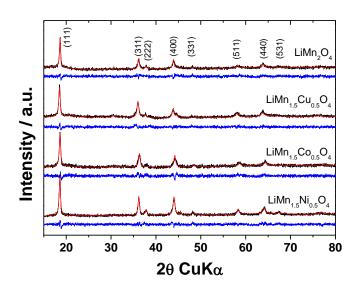205 all the structures [22].

206

207 **Figure 3-** Refined powder XRD patterns fits (black curve – experimental; red curve –
208 calculated; blue curve – difference plot) for $LiMn_2O_4$ and $LiMn_{1.5}M_{0.5}O_4$ (M: Ni, Cu, Co)
209 doped particles.

The results show that the Ni-, Cu- and Co-doping does not influence the symmetry of the spinel structure of the $LiMn_2O_4$ and present a cubic close-packed (ccp) sublattice, where O-ion occupies the 32e site, Li-ion occupies the tetrahedral 8a site and the Mn-ions (Mn^{3+}/Mn^{4+}) the octahedral 16d site [23]. The doped-ions (Ni, Cu and Co) also occupy the octahedral 16d site [23-25]. The (400) peak presents high intensity for the $LiMn_2O_4$ and $LiMn_{1.5}Ni_{0.5}O_4$ samples and, as shown in Table 2, the intensity relation between the (311) and (400) peak are lower at these samples. As reported [26], the progressive addition of doping elements in the $LiMn_2O_4$ structure leads to an increase in the intensity ratio of (311)/(400) peaks. While the (311)/(400) ratios of Cu- and Co- doped samples show increased values, the same ratio in the Ni-doped sample is apparently lower. Since the increase of this ratio is associated with increased substitution of the tetrahedral site (8a), this means that in Ni-doped sample the isomorphous substitution is probably more efficient in the octahedral 16d site, replacing the Mn^{3+} ion [27]. It was also found that the lattice parameter decreases with the addition of the studied doped elements (Table 2) which may be attributed to the partial substitution of Mn^{3+} [25] and creation of structural defects.
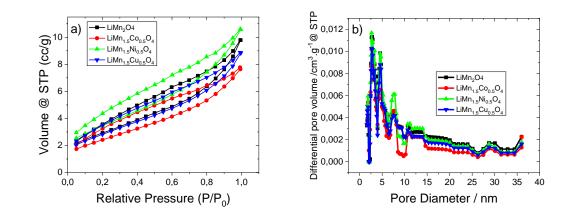
Table 2 - XRD structural parameters for $LiMn_2O_4$, $LiMn_{1.5}M_{0.5}O_4$ (M: Ni, Cu, Co).

Sample description	Lattice parameters /Å	Unit cell volume / Å³	$I_{(311)/(400)}$
$LiMn_2O_4$	8.25	560.6	1.22
$LiMn_{1.5}Ni_{0.5}O_4$	8.20	551.0	1.21
$LiMn_{1.5}Cu_{0.5}O_4$	8.24	560.6	1.60
$LiMn_{1.5}Co_{0.5}O_4$	8.15	542.2	1.53

The surface area and porosity of each particle were studied by nitrogen adsorption-desorption characterization. The respective nitrogen adsorption isotherms and pore size distribution are shown in Figure 4a and Figure 4b, respectively. The studied particles exhibit a mesoporous polyhedral crystal structure with slightly different specific surface areas (Table 3). The surface area was evaluated by multi-point BET method and results of 11, 10, 12 and 9 m^2 g^{-1} were obtained for $LiMn_2O_4$, $LiMn_{1.5}Ni_{0.5}O_4$, $LiMn_{1.5}Cu_{0.5}O_4$, and $LiMn_{1.5}Co_{0.5}O_4$, respectively.

236

237

Figure 4 - a) N_2 adsorption - desorption isotherms and b) pore size distribution for LiMn$_2$O$_4$ and LiMn$_{1.5}$M$_{0.5}$O$_4$ (M: Ni, Cu, Co).

Average pore size distribution results show a pore size distribution between 2 and 37 nm, which indicate a heterogeneous surface morphology. LiMn$_2$O$_4$ exhibits a higher average pore size of 2.9 nm and, after doping with Ni, Cu and Co, the average pore size of the samples decreases to 2.6 nm (Table 3). Comparing the surface area with the pore size distribution, it can be concluded that the doped samples show different agglomeration characteristics. LiMn$_{1.5}$Co$_{0.5}$O$_4$ particles show higher agglomeration due to low surface area for the same pore size than the other doped samples. These results are also supported by the SEM and TEM images shown in Figure 1.

Table 3 - BET parameters of LiMn$_2$O$_4$ and LiMn$_{1.5}$M$_{0.5}$O$_4$ (M: Ni, Cu, Co).

	BET parameters	
Sample description	**Surface area / m^2 g^{-1}**	**Average pore size / nm**
LiMn$_2$O$_4$	11	2.9
LiMn$_{1.5}$Ni$_{0.5}$O$_4$	10	2.6
LiMn$_{1.5}$Cu$_{0.5}$O$_4$	12	2.6
LiMn$_{1.5}$Co$_{0.5}$O$_4$	9	2.6

249

250   Thermal stability of $LiMn_2O_4$ and $LiMn_{1.5}M_{0.5}O_4$ (M: Ni, Cu, Co) particles was analyzed

251   by TGA and the results are shown in Figure 5a. Comparing the results, all the particles

252   present a weight loss between the 700 °C and 900 °C due to the oxygen loss and the

253   formation of a $LiMn_2O_{4+x}$ structure [28]. It can be observed that the addition of the doping

254   elements (Ni, Cu, Co) in the $LiMn_2O_4$ structure stabilizes its thermal degradation around

255   5% until 700 °C. This behavior was already observed for doping with rare-earth elements
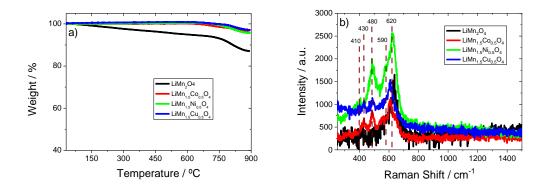
256   (Gd, Yb, Tb and Dy) [21].

258   **Figure 5 -** a) TGA analysis and b) Raman spectra of $LiMn_2O_4$ and $LiMn_{1.5}M_{0.5}O_4$ (M:

259   Ni, Cu, Co).

261    $LiMn_2O_4$ and $LiMn_{1.5}M_{0.5}O_4$ (M: Ni, Cu, Co) particles were studied by Raman

262   spectroscopy (Figure 5b). The common spectra of manganese oxides reveal a strong band

263   around 620 cm^{-1}, which is the characteristic vibration of the oxygen atoms inside the

264   octahedral MnO_6 unit [29]. The results show this strong band around 620 cm^{-1} for all the

265   studied particles, assigned to the A_{1g} species in O_h^7 spectroscopic symmetry [30]. Other

266   less intense bands at 590, 480, 430 and 410 cm^{-1} were also found and are related to the

267   T_{2g} mode from the symmetric bending vibration of Mn-O bond, T_{2g} phase, E_g vibration

268   and E_g vibration, respectively, of the Fd-3m space group [31, 32].

270   *3.2. Electrochemical studies of the cathodes*

271   The electrochemical properties of the $LiMn_2O_4$ and $LiMn_{1.5}M_{0.5}O_4$ (M: Ni, Cu, Co)

272   cathodes are represented in Figures 6 and 7. The room temperature fifth charge/discharge

273   curve profiles of the $LiMn_{1.5}Ni_{0.5}O_4$ cathode as a function of different C-rates between

274   3.5 and 4.9 V, are presented in Figure 6a. The other samples present the same type of

275 curve profile. Two curves for each C-rate are shown, which are characterized by the

276 charge and discharge curves originated by the lithium disinsertion and insertion,
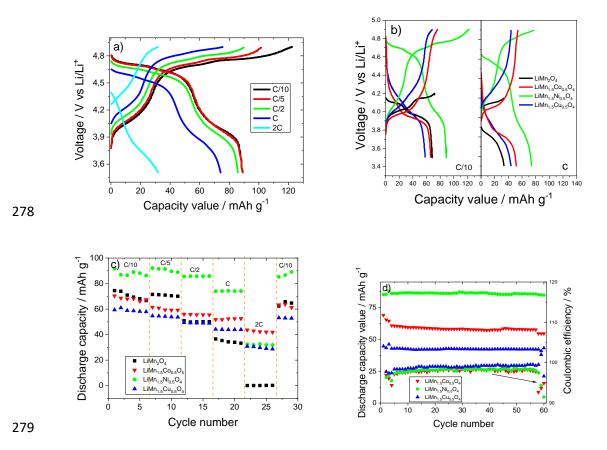
277 respectively, in the cathode structure.

278

279

280 **Figure 6 -** a) Fifth charge/discharge curves of $LiMn_{1.5}Ni_{0.5}O_4$ between C/10- and 2C-

281 rate, b) fifth charge/discharge curves of the different studied samples at a C/10- and C-

282 rate, c) rate performance discharge process of the different studied samples between

283 C/10- and 2C-rate and d) cycling performance of the different samples at C-rate during

284 60 cycles.

285 It is observed for $LiMn_{1.5}Ni_{0.5}O_4$ cathodes (Figure 6a) different plateaus at 4.0 V due to

286 the Mn^{4+}/Mn^{3+} reduction, at 4.6 V due to Ni^{3+}/Ni^{2+} reduction and at 4.7 V due to Ni^{4+}/Ni^{3+}

287 reduction [33-36]. Furthermore, those plateaus are formed by the lithium-ion insertion

288 into the 16C octahedral (plateau at 4.0 V) and 8a tetrahedral (plateau at 4.6 V and 4.7 V)

289 sites of the spinel structure. Discharge capacity values of 89, 89, 86, 74 and 32 mAh g^{-1}

290 at C/10, C/5, C/2, C and 2C, respectively, were obtained. Also, it is verified that the

291 cycling profile decreases with increasing current rates. The difference in capacity at the

292 C/10 rate is explained by the ohmic polarization effect and by the formation of the solid

293   electrolyte interface (SEI) layer in the first cycles [37]. Also, the typical irreversibility at

294   low scan rates between charge and discharge is verified at C/10-rate [37].

295     $LiMn_2O_4$ and $LiMn_{1.5}M_{0.5}O_4$ (M: Ni, Cu, Co) cathodes fifth charge/discharge curves

296   obtained at C/10- and C-rate at room temperature are presented in Figure 6b. The

297   discharge capacity values of 68, 89, 58 and 66 mAh g^{-1} at C/10-rate and 34, 74, 44 and

298   52 mAh g^{-1} at C-rate for $LiMn_2O_4$, $LiMn_{1.5}Ni_{0.5}O_4$, $LiMn_{1.5}Cu_{0.5}O_4$ and $LiMn_{1.5}Co_{0.5}O_4$

299   cathodes, were respectively obtained. The observed different voltage cutoff between the

300     $LiMn_{1.5}Ni_{0.5}O_4$, and the rest of the samples is due to the presence Ni^{3+}/Ni^{2+} reduction at

301   4.6 V and Ni^{4+}/Ni^{3+} reduction at 4.7 V. The other samples show the plateau at 4.1 V that

302   corresponds to the reduction of Mn^{4+} to Mn^{3+}. It is thus observed that the doping process

303   with Ni, Cu and Co influence the charge and discharge performance of $LiMn_2O_4$ cathodes.

304   Furthermore, doping reduced the decrease of the specific discharge capacity with

305   increasing C-rate. Doping process also induces a slight reduction in the particle size, as

306   mentioned before in section 3.1, leading to an enhancement of the electrochemical

307   performance of these cathodes. This lower size of the particles influences the insertion

308   and disinsertion of lithium-ions in the cathode active material structure, increasing the

309   specific discharge capacity due to their larger surface area. Typically, cathode materials

310   that are in the 4 V potential range have surface areas near to 3 $m^2.g^{-1}$ [38]. The obtained

311   lower electrochemical results, compared with other works [38-41], can be thus also

312   explained by the higher particle surface area of the materials used in the present work

313   (Table 3). With the increase of current rates, the plateau voltages between the charge and

314   discharge increase and decrease, respectively, due to the increased cell polarization, as

315   well the gradually blurry of the two plateaus [42]. In the present study, these changes are

316   also observed, but with less intensity for the $LiMn_{1.5}Ni_{0.5}O_4$ cathode. Comparing the

317   studied cathodes, $LiMn_{1.5}Ni_{0.5}O_4$ and $LiMn_{1.5}Cu_{0.5}O_4$ cathodes possess higher specific

318   discharge capacity when cycled at a high rate (C-rate).

319   Figure 6c shows the discharge rate performance, of all prepared cathodes, during the

320   cycling process. All the samples present good cycling stability in almost all applied rates.

321   It is observed a decrease of the specific discharge capacity with increasing rates for all

322   the tested cathodes, being more marked for the $LiMn_2O_4$ cathode. Although that, it was

323   verified that all the samples present excellent recovery specific discharge capacity at C/10

324   rate. The doping of Ni, Cu and Co into $LiMn_2O_4$, clearly enhances the specific discharge

325   capacity compared with non-doped $LiMn_2O_4$, at high rate. At low rates, the sample with

326   the Ni doping presents the highest specific discharge capacity. Specific discharge

327   capacities of 33, 74, 44 and 53 mAh g^{-1} (at C) and 74, 89, 59 and 69 mAh g^{-1} (at C/10)

328   were obtained for LiMn$_2$O$_4$, LiMn$_{1.5}$Ni$_{0.5}$O$_4$, LiMn$_{1.5}$Cu$_{0.5}$O$_4$ and LiMn$_{1.5}$Co$_{0.5}$O$_4$

329   cathodes, respectively. The exchange between the Mn^{3+} ion of the LiMn$_2$O$_4$ spinel

330   structure and the doped elements, promotes higher electrochemical performance of the

331   cathodes with doped active material particles [43]. Furthermore, the low intensity of the

332   ratio of (311)/(400) planes for the LiMn$_{1.5}$Ni$_{0.5}$O$_4$ cathode and its low lattice parameter

333   suggest to be the reason for such cathode presenting higher electrochemical performance

334   among all studied cathodes.

335   Figure 6d presents the cycle stability of the doped cathodes. It is shown the stability of

336   the doped cathodes at C-rate during 60 cycles at room temperature. The obtained specific

337   discharge capacity was 85, 43 and 55 mAh g^{-1} (at 60th cycle) for LiMn$_{1.5}$Ni$_{0.5}$O$_4$,

338   LiMn$_{1.5}$Cu$_{0.5}$O$_4$ and LiMn$_{1.5}$Co$_{0.5}$O$_4$ cathodes, respectively. It was also calculated the

339   coulombic efficiency percentage, that is approximately 100 %, demonstrating the good

340   electrochemical stability of all the samples. Capacity fade percentage (2nd to 50th cycles)

341   were 0.5, 3.1 and 21.0 % for LiMn$_{1.5}$Ni$_{0.5}$O$_4$, LiMn$_{1.5}$Cu$_{0.5}$O$_4$ and LiMn$_{1.5}$Co$_{0.5}$O$_4$

342   cathodes, respectively, showing once again the good electrochemical performance of

343   LiMn$_{1.5}$Ni$_{0.5}$O$_4$, due to its low capacity fade over cycling. The high capacity fade of the

344   LiMn$_{1.5}$Co$_{0.5}$O$_4$ cathode can be associated to the higher active material particle

345   agglomeration confirmed by the BET analysis, decreasing its cycling performance [44].

346   The low capacity fade of the LiMn$_{1.5}$Ni$_{0.5}$O$_4$ cathode also suggests the good substitution

347   of Mn by Ni at the octahedral 16d site [45], as confirmed by the XRD results.

348   The electrochemical impedance spectroscopy (EIS) of the studied cathodes were

349   evaluated before and after cycling and the results are presented in Figure 7a and 7b,
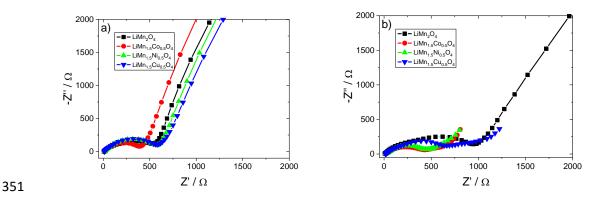
350   respectively.

351

Figure 7 – EIS spectra for the different batteries a) before and b) after cycling.

The impedance spectra of the samples is characterized by two semicircles in the high/medium frequency region followed by a straight line at the low-frequency region. The mentioned semicircles are characteristics of the resistance contribution. These resistances are described by ohmic resistance, that represents the liquid/electrolyte resistance, obtained by the intercept with the Z' at high frequencies; surface resistance (R_s), represented by the first semicircle and is described by the resistance of the solid/electrolyte interface (SEI); and the charge-transfer resistance process (R_{ct}) that is defined by the second semicircle [46]. The mentioned straight line at low frequencies represents the Warburg impedance that is correlated to the lithium-ion diffusion in the bulk material [46]. Comparing both EIS spectra (before and after cycling), it is observed that the doping process does not influence the shape of the curves. Also, a total resistance increases after half-cells cycling has been observed for all samples, excepting for the $LiMn_{1.5}Ni_{0.5}O_4$ cathode. The obtained total resistances for the half-cells is presented in Table 4.

Table 4: Total resistance values obtained for the prepared cathodic half-cells, before and after cycling.

Sample	Total Resistance, R_{total} / Ω	
	Before cycling	**After cycling**
$LiMn_2O_4$	532.5	951.8
$LiMn_{1.5}Co_{0.5}O_4$	389.8	429.7
$LiMn_{1.5}Ni_{0.5}O_4$	570.3	439.9
$LiMn_{1.5}Cu_{0.5}O_4$	580.3	666.3

The change of the total resistances after cathodic half-cells cycling is related to SEI formation [47]. For the $LiMn_{1.5}Ni_{0.5}O_4$ cathode, the SEI formation decreases the total half-cell resistance, which is the opposite behavior as in the other cells. Thus, higher conducting solid/electrolyte interface is formed in this sample, provably related to the more efficient substitution of Mn^{3+} by Ni and the corresponding structural particle modifications, which improves electrochemical charge/discharge performance.

4. Conclusions

378 A sol-gel synthesis was successfully used to produce $LiMn_2O_4$ and $LiMn_{1.5}M_{0.5}O_4$ (M:

379 Ni, Cu, Co) doped particles with a size range between 50 and 200 nm. Particles show

380 similar stoichiometric ratio of the doped elements and lattice fringes between 0.47 and

381 0.48 nm for the single crystalline domains doped particles. Doped elements also occupy

382 the octahedral 16d site, where the Ni shows a more efficient substitution, replacing the

383 Mn^{3+} ion and therefore improving the drawback of poor cycling behavior of $LiMn_2O_4$.

384 Doped particles show higher thermal stability between 700 and 900 °C and high

385 crystallinity. Electrochemical performance in cathodic half-cells show discharge

386 capacities of 33, 74, 44 and 53 mAh g^{-1} (at C) for $LiMn_2O_4$, $LiMn_{1.5}Ni_{0.5}O_4$,

387 $LiMn_{1.5}Cu_{0.5}O_4$ and $LiMn_{1.5}Co_{0.5}O_4$ cathodes, respectively. Further, an excellent

388 coulombic coefficient percentage (around 100 %) was observed for all doped cathodes.

389 A capacity fade percentage of 0.5, 3.1 and 21.0 % for $LiMn_{1.5}Ni_{0.5}O_4$, $LiMn_{1.5}Cu_{0.5}O_4$ and

390 $LiMn_{1.5}Co_{0.5}O_4$ cathodes were respectively obtained, showing the good electrochemical

391 performance of $LiMn_{1.5}Ni_{0.5}O_4$. Furthermore, the $LiMn_{1.5}Ni_{0.5}O_4$ cathode shows a

392 decrease in the total half-cell resistance after cycling. The transition metal synthetized

393 particles show to be suitable for being used as a cathode in lithium-ion batteries based on

394 their excellent electrochemical stability.

395

396 **Declaration of competing interest**

397 The authors declare no competing financial interest.

398

399

408   REFERENCES

409   [1] A. Eftekhari, ACS Sustainable Chemistry & Engineering, 5 (2017) 2799-2816.
410   https://doi.org/10.1021/acssuschemeng.7b00046
411   [2] J. Ma, P. Hu, G. Cui, L. Chen, Chemistry of Materials, 28 (2016) 3578-3606.
412   https://doi.org/10.1021/acs.chemmater.6b00948
413   [3] M.S. Whittingham, Chemical Reviews, 104 (2004) 4271-4302.
414   https://doi.org/10.1021/cr020731c
415   [4] B. Writer, in Cathode Materials, Samples, Pristine, Layered, Doping, Discharge Capacity, pp.
416   73-161, Springer International Publishing, Cham (2019).
417   [5] N. Nitta, F. Wu, J.T. Lee, G. Yushin, Materials Today, 18 (2015) 252-264.
418   https://doi.org/10.1016/j.mattod.2014.10.040
419   [6] B. Put, P.M. Vereecken, N. Labyedh, A. Sepulveda, C. Huyghebaert, I.P. Radu, A. Stesmans,
420   ACS Applied Materials & Interfaces, 7 (2015) 22413-22420.
421   https://doi.org/10.1021/acsami.5b06386
422   [7] Y.J. Wei, L.Y. Yan, C.Z. Wang, X.G. Xu, F. Wu, G. Chen, The Journal of Physical Chemistry B,
423   108 (2004) 18547-18551. https://doi.org/10.1021/jp0479522
424   [8] I. Taniguchi, D. Song, M. Wakihara, Journal of Power Sources, 109 (2002) 333-339.
425   https://doi.org/10.1016/S0378-7753(02)00076-9
426   [9] D. Tang, L. Ben, Y. Sun, B. Chen, Z. Yang, L. Gu, X. Huang, Journal of Materials Chemistry A, 2
427   (2014) 14519-14527. https://doi.org/10.1039/C4TA02109F
428   [10] J.-Y. Luo, H.-M. Xiong, Y.-Y. Xia, The Journal of Physical Chemistry C, 112 (2008) 12051-
429   12057. https://doi.org/10.1021/jp800915f
430   [11] C. Zhang, X. Liu, Q. Su, J. Wu, T. Huang, A. Yu, ACS Sustainable Chemistry & Engineering, 5
431   (2017) 640-647. https://doi.org/10.1021/acssuschemeng.6b02011
432   [12] L. Su, P.M. Smith, P. Anand, B. Reeja-Jayan, ACS Applied Materials & Interfaces, 10 (2018)
433   27063-27073. https://doi.org/10.1021/acsami.8b08711
434   [13] M. Okubo, Y. Mizuno, H. Yamada, J. Kim, E. Hosono, H. Zhou, T. Kudo, I. Honma, ACS Nano,
435   4 (2010) 741-752. https://doi.org/10.1021/nn9012065
436   [14] B. Deng, H. Nakamura, Q. Zhang, M. Yoshio, Y. Xia, Electrochimica Acta, 49 (2004) 1823-
437   1830. https://doi.org/10.1016/j.electacta.2003.11.032
438   [15] Q. Jiang, D. Liu, H. Zhang, S. Wang, The Journal of Physical Chemistry C, 119 (2015) 28776-
439   28782. https://doi.org/10.1021/acs.jpcc.5b10298
440   [16] W. Zhang, D.M. Cupid, P. Gotcu, K. Chang, D. Li, Y. Du, H.J. Seifert, Chemistry of Materials,
441   30 (2018) 2287-2298. https://doi.org/10.1021/acs.chemmater.7b05068
442   [17] Y.-K. Sun, D.-W. Kim, Y.-M. Choi, Journal of Power Sources, 79 (1999) 231-237.
443   https://doi.org/10.1016/S0378-7753(99)00160-3
444   [18] S. Huang, B.E. Wilson, W.H. Smyrl, D.G. Truhlar, A. Stein, Chemistry of Materials, 28 (2016)
445   746-755. https://doi.org/10.1021/acs.chemmater.5b03554
446   [19] P. Ram, A. Gören, R. Gonçalves, G. Choudhary, S. Ferdov, M.M. Silva, R. Singhal, C.M.
447   Costa, R.K. Sharma, S. Lanceros-Méndez, Composites Part B: Engineering, 139 (2018) 55-63.
448   https://doi.org/10.1016/j.compositesb.2017.11.054
449   [20] Y. Xue, L.-L. Zheng, J. Wang, J.-G. Zhou, F.-D. Yu, G.-J. Zhou, Z.-B. Wang, ACS Applied
450   Energy Materials, 2 (2019) 2982-2989. https://doi.org/10.1021/acsaem.9b00564
451   [21] P. Ram, A. Gören, S. Ferdov, M.M. Silva, R. Singhal, C.M. Costa, R.K. Sharma, S. Lanceros-
452   Méndez, New Journal of Chemistry, 40 (2016) 6244-6252. https://doi.org/10.1039/C6NJ00198J
453   [22] X. Zhang, F. Cheng, K. Zhang, Y. Liang, S. Yang, J. Liang, J. Chen, RSC Advances, 2 (2012)
454   5669-5675. https://doi.org/10.1039/C2RA20669B
455   [23] C.M. Julien, A. Mauger, K. Zaghib, H. Groult, Inorganics, 2 (2014) 132-154.
456   [24] T.-F. Yi, J. Mei, Y.-R. Zhu, Journal of Power Sources, 316 (2016) 85-105.
457   https://doi.org/10.1016/j.jpowsour.2016.03.070

458 [25] L. Liang, M. Xiang, W. Bai, J. Guo, C. Su, L. Yang, H. Bai, X. Liu, Journal of Materials Science:
459 Materials in Electronics, 31 (2020) 286-297. https://doi.org/10.1007/s10854-019-02502-7
460 [26] H. Zhao, F. Li, X. Liu, C. Cheng, Z. Zhang, Y. Wu, W. Xiong, B. Chen, Electrochimica Acta, 151
461 (2015) 263-269. https://doi.org/10.1016/j.electacta.2014.11.095
462 [27] M.-C. Yang, B. Xu, J.-H. Cheng, C.-J. Pan, B.-J. Hwang, Y.S. Meng, Chemistry of Materials, 23
463 (2011) 2832-2841. https://doi.org/10.1021/cm200042z
464 [28] D.G. Fauteux, A. Massucco, J. Shi, C. Lampe-O¨Nnerud, Journal of Applied
465 Electrochemistry, 27 (1997) 543-549. https://doi.org/10.1023/A:1018494511418
466 [29] C.V. Ramana, M. Massot, C.M. Julien, Surface and Interface Analysis, 37 (2005) 412-416.
467 https://doi.org/10.1002/sia.2022
468 [30] S.R.S. Prabaharan, N.B. Saparil, S.S. Michael, M. Massot, C. Julien, Solid State Ionics, 112
469 (1998) 25-34. https://doi.org/10.1016/S0167-2738(98)00219-7
470 [31] B. Slautin, D. Alikin, D. Rosato, D. Pelegov, V. Shur, A. Kholkin, 4 (2018) 21.
471 [32] B. Ammundsen, G.R. Burns, M.S. Islam, H. Kanoh, J. Rozière, The Journal of Physical
472 Chemistry B, 103 (1999) 5175-5180. https://doi.org/10.1021/jp984398l
473 [33] S. Mandal, R.M. Rojas, J.M. Amarilla, P. Calle, N.V. Kosova, V.F. Anufrienko, J.M. Rojo,
474 Chemistry of Materials, 14 (2002) 1598-1605. https://doi.org/10.1021/cm011219v
475 [34] T. Huang, X. Zheng, Y. Pan, Q. Li, M. Wu, ACS Applied Materials & Interfaces, 11 (2019)
476 26872-26879. https://doi.org/10.1021/acsami.9b07126
477 [35] H. Liu, J. Wang, X. Zhang, D. Zhou, X. Qi, B. Qiu, J. Fang, R. Kloepsch, G. Schumacher, Z. Liu,
478 J. Li, ACS Applied Materials & Interfaces, 8 (2016) 4661-4675.
479 https://doi.org/10.1021/acsami.5b11389
480 [36] D.W. Shin, C.A. Bridges, A. Huq, M.P. Paranthaman, A. Manthiram, Chemistry of Materials,
481 24 (2012) 3720-3731. https://doi.org/10.1021/cm301844w
482 [37] G. Gabrielli, M. Marinaro, M. Mancini, P. Axmann, M. Wohlfahrt-Mehrens, Journal of
483 Power Sources, 351 (2017) 35-44. https://doi.org/10.1016/j.jpowsour.2017.03.051
484 [38] X. Qin, J. Gong, J. Guo, B. Zong, M. Zhou, L. Wang, G. Liang, Journal of Alloys and
485 Compounds, 786 (2019) 240-249. https://doi.org/10.1016/j.jallcom.2019.01.307
486 [39] Y. Yu, M. Xiang, J. Guo, C. Su, X. Liu, H. Bai, W. Bai, K. Duan, Journal of Colloid and Interface
487 Science, 555 (2019) 64-71. https://doi.org/10.1016/j.jcis.2019.07.078
488 [40] J. Wang, Y.-y. Yu, B.-h. Wu, W.-q. Lin, J.-y. Li, J.-b. Zhao, Journal of Materials Chemistry A, 3
489 (2015) 2353-2360. 10.1039/C4TA05311G
490 [41] J. Betz, L. Nowak, J.-P. Brinkmann, P. Bärmann, M. Diehl, M. Winter, T. Placke, R. Schmuch,
491 Electrochimica Acta, 325 (2019) 134901. https://doi.org/10.1016/j.electacta.2019.134901
492 [42] Y. Deng, Y. Zhou, Z. Shi, X. Zhou, X. Quan, G. Chen, Journal of Materials Chemistry A, 1
493 (2013) 8170-8177. https://doi.org/10.1039/C3TA11563A
494 [43] G. Cherkashinin, D. Ensling, W. Jaegermann, Journal of Materials Chemistry A, 2 (2014)
495 3571-3580. https://doi.org/10.1039/C3TA14509C
496 [44] W.-R. Liu, Z.-Z. Guo, W.-S. Young, D.-T. Shieh, H.-C. Wu, M.-H. Yang, N.-L. Wu, Journal of
497 Power Sources, 140 (2005) 139-144. https://doi.org/10.1016/j.jpowsour.2004.07.032
498 [45] Y.-S. Lee, N. Kumada, M. Yoshio, Journal of Power Sources, 96 (2001) 376-384.
499 https://doi.org/10.1016/S0378-7753(00)00652-2
500 [46] X. Tang, J. Zhou, M. Bai, W. Wu, S. Li, Y. Ma, Journal of Materials Chemistry A, 7 (2019)
501 13364-13371. https://doi.org/10.1039/C9TA02718A
502 [47] D.W. Shin, A. Manthiram, Electrochemistry Communications, 13 (2011) 1213-1216.
503 https://doi.org/10.1016/j.elecom.2011.08.041

504